Anisotropic phonon-mediated electronic transport in chiral Weyl semimetals

Christina A. C. Garcia, Dennis M. Nenno, Georgios Varnavides, and Prineha Narang

Phys. Rev. Materials **5**, L091202 — Published 27 September 2021

DOI: 10.1103/PhysRevMaterials.5.L091202

Anisotropic phonon-mediated electronic transport in chiral Weyl semimetals

Christina A. C. Garcia,[1] Dennis M. Nenno,[1,2] Georgios Varnavides,[1,3] and Prineha Narang[1,*]

[1]*John A. Paulson School of Engineering and Applied Sciences, Harvard University, Cambridge, MA 02138, USA*
[2]*Max Planck Institute for Chemical Physics of Solids, 01187 Dresden, Germany*
[3]*Department of Materials Science and Engineering, Massachusetts Institute of Technology, Cambridge, MA 02139, USA*

(Dated: September 9, 2021)

Discovery and observations of exotic, quantized optical and electrical responses have sparked renewed interest in nonmagnetic chiral crystals. Within this class of materials, six group V transition metal ditetrelides, that is, XY_2 (X = V, Nb, Ta and Y = Si, Ge), host composite Weyl nodes on high-symmetry lines, with Kramers-Weyl fermions at time-reversal invariant momenta. In addition, at least two of these materials, $NbGe_2$ and $NbSi_2$, exhibit superconducting transitions at low temperatures. The interplay of strong electron-phonon interaction and complex Fermi surface topology present an opportunity to study both superconductivity and hydrodynamic electron transport in these systems. Towards this broader question, we present an *ab initio* theoretical study of the electronic transport and electron-phonon scattering in this family of materials, with a particular focus on $NbGe_2$ vs. $NbSi_2$, and the other group V ditetrelides. We shed light on the microscopic origin of $NbGe_2$'s large and anisotropic room temperature resistivity and contextualize its strong electron-phonon scattering with a presentation of other relevant scattering lifetimes, both momentum-relaxing and momentum-conserving. Our work explores the intriguing possibility of observing hydrodynamic electron transport in these chiral Weyl semimetals.

I. INTRODUCTION

Structurally chiral crystals have gained renewed attention, as they can realize Kramers-Weyl fermions at high-symmetry points of the band structure [1–3]. Crystals that lack inversion, mirror or rotoinversion symmetries are intrinsically chiral, and it has been theoretically suggested that in nonmagnetic compounds which belong to chiral space groups, all crossing points at time-reversal invariant momenta (TRIM) in the electronic band structure carry a topological charge [1, 2]. In systems where these topological bands dominate the electrical and optical response, a number of exciting phenomena have been proposed, such as nonlocal and nonreciprocal electron transport [1, 4] and a large quantized circular photogalvanic effect at room temperature [5].

Here, we investigate electronic transport in all transition metal ditetrelides, that is, XY_2 (X = V, Nb, Ta and Y = Si, Ge), known to crystallize in the non-symmorphic hexagonal chiral space group $P6_222$ (no. 180) or $P6_422$ (no. 181), with a particular focus on $NbSi_2$ and $NbGe_2$. Transition metal disilicides (Y = Si) have a rich literature primarily due to their low resistivity and possible application as silicon contacts [6–8]. Their thermal and electrical properties have been studied in technological contexts [6, 8–12], and their structural stability and electronic properties ranging from the superconducting transition and up to room temperature have also been investigated [10, 11, 13]. The experimental focus in group V digermanides (Y = Ge) has been driven by the low-temperature superconductivity exhibited by thin films and single crystals [14]. They have been studied as potential high-temperature structural materials, in particular $NbGe_2$ with its type-I to type-II superconducting transition around 2 K and extremely high residual-resistance ratio in clean samples [14–17]. The combination of topological band character together with low-temperature superconductivity presents this whole family of materials as an intriguing playground for fundamental questions in the strength of electron-phonon coupling in condensed matter.

Our study explores the anisotropic electronic transport properties of group V transition metal disilicides and digermanides through first principles calculations, incorporating the interactions between electronic and phononic states. In particular, we compute the intrinsic resistivities of these materials as functions of temperature, as they arise from electron-phonon interactions, and explore their respective possibilities for observing a hydrodynamic transport regime. We focus on the near order of magnitude higher resistivity in $NbGe_2$ compared to other group V ditetrelides at high temperatures. We trace this difference back to the pronounced scattering at the Fermi surface, which is energetically favored for certain stoichiometry. The strong electron-phonon interaction in $NbGe_2$ – the origin of high room-temperature resistivity – serves as a motivation to study the possibility of observing hydrodynamic transport induced by extremely short-lived, phonon-mediated electron-electron scattering events in this material. We predict the hydrodynamic electron flow in microscale devices of $NbGe_2$ of comparable size to be even more pronounced than in the recently reported Poiseuille flow observed in WTe_2 [18] wires.

II. MATERIALS AND METHODS

All six transition metal ditetrelides show stable phases in both the nonsymmorphic Sohnke space group $P6_222$

* prineha@seas.harvard.edu

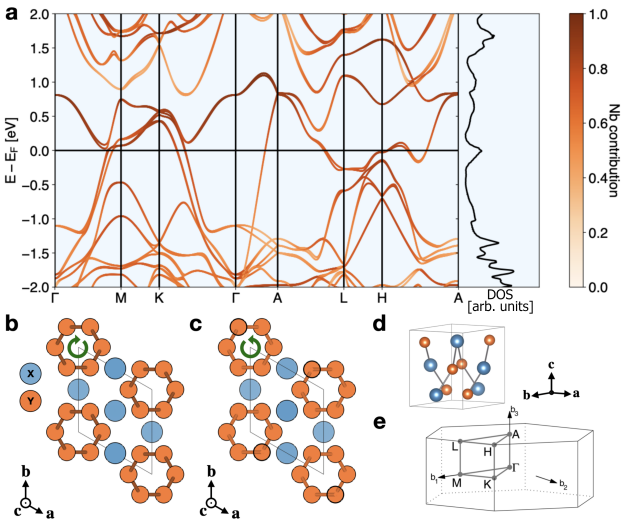

Figure 1. (a) Electronic band structure (left panel) and density of states (right panel) of $NbGe_2$ in space groups 180 and 181 color-coded by Nb-contribution to the bands. The unit cell of $NbGe_2$ in space group 180 (b) and spacegroup 181 (c) is displayed viewed along the c-axis and from the side (d). (e) Brillouin zone of the hexagonal unit cell with high-symmetry paths (from Ref. 19).

(no. 180) and its energy-degenerate enantiomorphic partner space group $P6_422$ (no. 181) and can be classified as enforced semimetals with Fermi degeneracy [16, 21, 22] The band structure for $NbGe_2$, shown in Fig. 1(a), coincides for both left- and right-handed chiralities of the unit cell (cf. Fig. 1(b,c)). All six compounds contain topologically nontrivial features in their electronic structure, owing to crystalline symmetries and strong spin-orbit coupling [1]. Kramers-Weyl nodes [23] are found at TRIM, i.e. the Γ, M, A and L points of the hexagonal Brillouin zone shown in Fig. 1(e). These degenerate crossings are enforced by the crystal symmetries, and the crossings closest to the Fermi surface appear at the M and H points in $NbGe_2$, where the dispersion becomes flat. Along the sixfold rotation symmetry axis Γ-A, band crossings with four-fold degeneracies occur, which are protected due to their opposite eigenvalues of the sixfold screw rotations $C_{6,2}$ [2, 3]. However, in all six compounds, these points lie more than 1 eV below the Fermi level, and only one doubly degenerate band crosses the Fermi surface along this line, which has a strong impact on the resistivity along $\hat{z}$. The band structure close to the Fermi level shows two pairs of bands split by spin-orbit coupling along the Γ-M axis, which lead to two doubly degenerate Kramers-Weyl points (chirality $|\chi| = 1$) on the TRIM. As observed in structurally-chiral PdGa, the chiral charge at each of these crossings flips sign between the enantiomorphic partners due to mirror symmetry [24]. Consequently, it is possible to distinguish the two enantiomers by their surface states. Due to bulk-surface correspondence, Fermi arcs form between Weyl points of opposite chirality.

In $NbGe_2$, a hole pocket emerges from unoccupied states at ∼5 meV above the Fermi level. The density of states, and thus the scattering state space at higher temperatures, increases drastically close to the bottom of this band and the Kramers-Weyl nodes in the vicinity of the Fermi level. While in the topological semimetal RhSi there exists a large energy window in the vicinity of the Fermi level in which topological degeneracies dominate and lead to a number of quantized responses, in $NbGe_2$, we do not expect Weyl points to dictate the electronic response [5, 25].

We compute the DC electrical resistivity tensor ρ from first principles using a linearized Boltzmann transport equation within a full-band relaxation time approximation incorporating state-resolved momentum-relaxing scattering lifetimes $\tau^{\mathrm{MR}}_{\text{e-ph}}(\mathbf{k}, n)$ and velocities $v_{n\mathbf{k}}$ (see Supplemental Material [20]),

$$\bar{\rho}^{-1} = \int_{\mathrm{BZ}} \frac{e^2 d\mathbf{k}}{(2\pi)^3} \sum_n \frac{\partial f_{n\mathbf{k}}}{\partial \varepsilon_{n\mathbf{k}}} (v_{n\mathbf{k}} \otimes v_{n\mathbf{k}})\, \tau^{\mathrm{MR}}_{\text{e-ph}}(\mathbf{k}, n), \quad (1)$$

where we integrate over all momenta $\mathbf{k}$ in the full Brillouin zone and sum over all electronic bands n, with $\varepsilon_{n\mathbf{k}}$ and $f_{n\mathbf{k}}$ being the electronic energies and occupations.

III. RESULTS AND DISCUSSION

A. Electrical Resistivities

The results for varying temperature in $NbGe_2$, $NbSi_2$, $TaGe_2$, and $TaSi_2$ are shown in Fig. 2(a), with available experimental data for $NbGe_2$, $NbSi_2$, and $TaSi_2$ overlaid [6, 14]. Similarly, for the vanadium ditetrelides we calculate $\rho_{xx} = 72.3\,\mu\Omega\,\mathrm{cm}$ and $\rho_{zz} = 38.4\,\mu\Omega\,\mathrm{cm}$ for VGe_2 and $\rho_{xx} = 58.1\,\mu\Omega\,\mathrm{cm}$ and $\rho_{zz} = 23.8\,\mu\Omega\,\mathrm{cm}$ for VSi_2 at room temperature. Since we only account for the contribution of momentum-relaxing electron-phonon scattering, we expect to underestimate the low-temperature resistivity unless the crystal is very clean, i.e. the scattering of electrons with impurities is negligible. This likely explains the mild underestimation seen for ρ_{zz} in $NbGe_2$ and $NbSi_2$ at lower temperatures. A slight overestimation of the resistivity, as seen for ρ_{xx} in $NbSi_2$ and $TaSi_2$ and ρ_{zz} in $TaSi_2$, can be explained by a misaligned Fermi level compared to the measured sample or slight differences in the lattice constants between our theoretical calculations and experiment. However, the overall excellent agreement with experiment indicates that the level of theory used is appropriate to capture the high-temperature behavior of the resistivity.

In comparing the high-temperature resistivities of these materials, we see that $NbGe_2$ stands out as having significantly larger resistivities along both a (xx) and c (zz) crystallographic directions, with ρ_{xx} and ρ_{zz} in $NbGe_2$ at room temperature being 3.7× and 1.6× those in VGe_2, which has the largest resistivities among the remaining

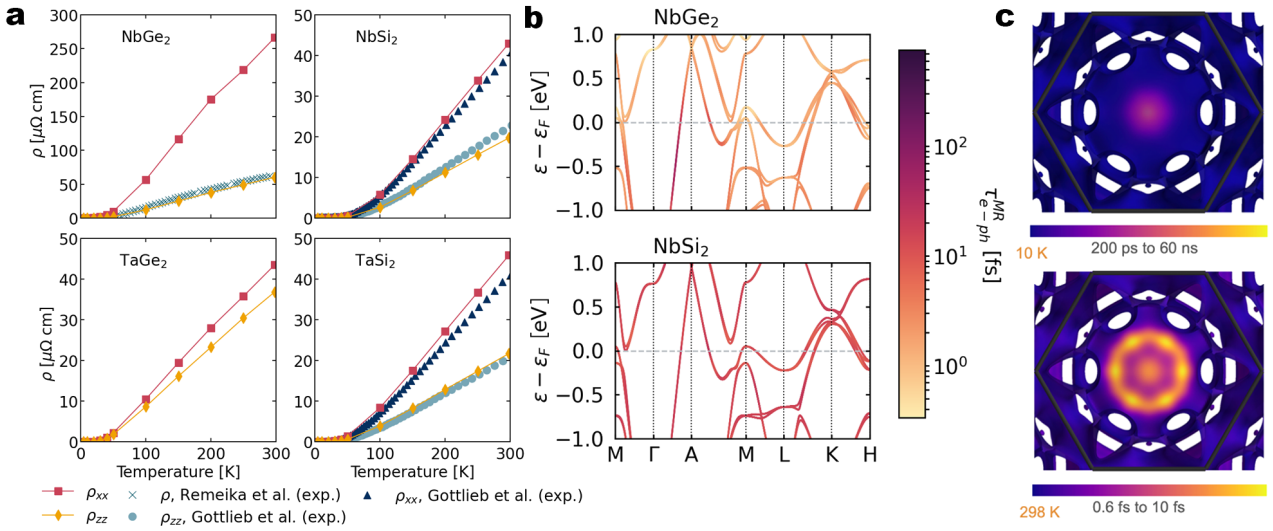

Figure 2. (a) Resistivity vs. temperature for $NbGe_2$, $NbSi_2$, $TaGe_2$, and $TaSi_2$. Experimental data by Remeika *et al.* [14] and Gottlieb *et al.* [6] are overlaid for comparison. (b) Computed room temperature momentum-relaxing electron-phonon lifetimes plotted on the electronic band structures of $NbGe_2$ and $NbSi_2$. While there are small variations in these lifetimes across the band structures for all six materials, the lifetimes of $NbGe_2$ are roughly an order of magnitude shorter than those of $NbSi_2$ and the other five materials (see Supplemental Material [20]), indicating stronger momentum-relaxing electron-phonon (e-ph) scattering. This stronger e-ph scattering can be explained by one to two orders of magnitude difference in the e-ph coupling. (c) The electron-phonon lifetimes plotted on the Fermi surface of $NbGe_2$ for 10 K and 298 K shown on the (0001)-surface. The hexagon marks the boundary of the first Brillouin zone.

five compounds. Only the in-plane resistivity has been accessed in experiments so far. $NbGe_2$ also has the largest anisotropy in resistivity between the a and c directions, with $\rho_{xx}/\rho_{zz} \approx 4.4$ at room temperature according to our predictions. Among the other group V transition metal ditetrelides, this ratio is 2.2, 1.2, 2.1, 1.9, and 2.4 for $NbSi_2$, $TaGe_2$, $TaSi_2$, VGe_2, and VSi_2, respectively. These results are surprising given that all six compounds considered here are isostructural and isoelectronic.

B. Electron-Phonon Scattering

To understand why the electrical resistivity of $NbGe_2$ at room temperature is so much larger and more anisotropic than the other group V transition metal ditetrelides, we analyze the main contributor to the resistivity, the momentum-relaxing electron-phonon scattering lifetime ($\tau^{\mathrm{MR}}_{\mathrm{e\text{-}ph}}$) (see Supplemental Material [20]). In Fig. 2(b), we present momentum- and energy-resolved $\tau^{\mathrm{MR}}_{\mathrm{e\text{-}ph}}$ along high-symmetry directions for $NbGe_2$ and $NbSi_2$ at room temperature. While there is noticeable variation in this lifetime across each band structure, it is apparent in comparing the two materials that this lifetime is roughly an order of magnitude shorter overall, i.e. across energy and momentum, in $NbGe_2$ compared to $NbSi_2$. This indicates that $NbGe_2$ has stronger momentum-relaxing electron-phonon scattering and helps to explain its comparatively larger resistivity, which is inversely proportional on the $\tau^{\mathrm{MR}}_{\mathrm{e\text{-}ph}}$, increasing with increased momentum-relaxing scattering.

In addition, we note that for the band intersecting the Fermi level along the k-path Γ-A in $NbGe_2$, $\tau^{\mathrm{MR}}_{\mathrm{e\text{-}ph}}$ is not as short as the same lifetime at other points that also cross the Fermi level; instead, it is comparable to the lifetimes calculated for $NbSi_2$ and the other transition metal ditetrelides (see Supplemental Material [20]). As transitions along Γ-A contribute primarily to ρ_{zz} and transitions along Γ-M contribute primarily to ρ_{xx}, the significant difference in momentum-relaxing scattering along these directions accounts for part of the large anisotropy we predict for $NbGe_2$. Separately, the increased scattering along M-L and K-H, which also contributes to ρ_{zz}, results in ρ_{zz} still being much larger in $NbGe_2$ than in the other five materials, despite the lesser scattering along Γ-M. These observations regarding the momentum-relaxing electron-phonon scattering lifetimes help to explain the resistivity results shown in Fig. 2(a).

We note, however, that the electronic band structures shown in Fig. 2 do not provide insight into momentum-relaxing scattering across the whole Fermi surface and thus must be regarded as a glimpse rather than a comprehensive picture. By contrast, Fig. 2(c) plots $\tau^{\mathrm{MR}}_{\mathrm{e\text{-}ph}}$ on the Fermi surface of $NbGe_2$ at 10 K and 298 K. At both temperatures, only part of the Fermi surface, with velocities along the z-axis, centered around the Γ point, shows the longest lifetimes, while other regions show lifetimes as low as 0.6 fs.

To better understand the order of magnitude difference in $\tau^{\mathrm{MR}}_{\mathrm{e\text{-}ph}}$ of $NbGe_2$ versus those of the other five group V transition metal ditetrelides, we compute the Fermi-

surface averaged electron-phonon interaction strength G (see Supplemental Material [20]) for different phonon wavevectors q and modes α. Using these, we plot the phonon-electron linewidths on the phonon dispersion plots for $NbGe_2$ and $NbSi_2$ in Fig. 3. The result provides microscopic insight into the anisotropy: while the modes that couple strongly, and thus lead to larger linewidth and increased resistivity, are highly-dependent on the phonon momentum direction in $NbGe_2$, the coupling in $NbSi_2$ appears to be more isotropic. In particular, the phonons that can transfer momentum in the crystallographic z-direction in $NbGe_2$ are almost exclusively weakly coupled, while phonons that can transfer electron momentum in-plane exhibit stronger couplings. A more detailed exposition of the electron-phonon coupling strength and its mode- and angular-dependence in $NbGe_2$ and $NbSi_2$ is presented in the Supplemental Material [20]. The order of magnitude difference in coupling strength between the two materials is further highlighted using the Eliashberg transfer function (Fig. 3 side panels).

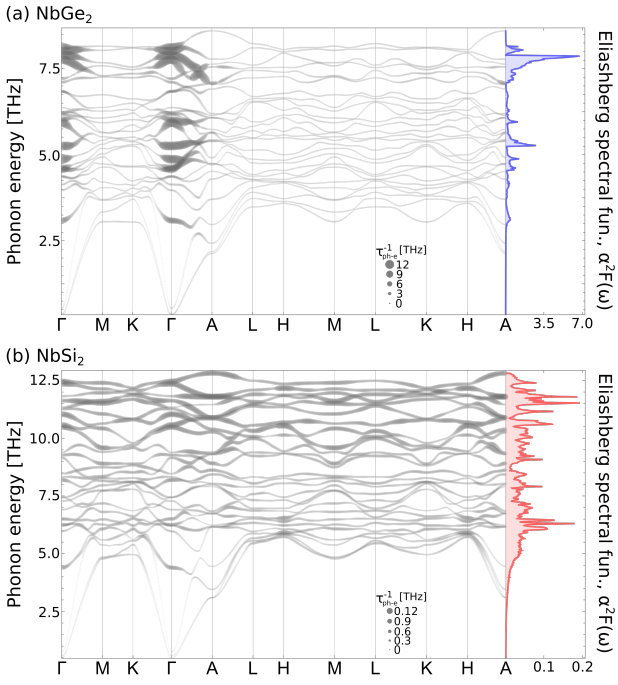

Figure 3. Phonon dispersion of **(a)** $NbGe_2$ and **(b)** $NbSi_2$ along the high symmetry path in the Brillouin zone (Fig. 1e), with the marker area indicating the imaginary part of phonon-electron self energy. The corresponding Eliashberg spectral function, $\alpha^2F(\omega)$ (see Supplemental Material Eq. (9)), is plotted as a function of frequency in the right panel. In contrast to $NbSi_2$, $NbGe_2$ presents a noticeable anisotropy, with the in-plane dispersion directions (Γ-M-K-Γ) exhibiting much larger phonon linewidths due to electron-phonon interactions. Further, we note the two orders of magnitude difference in the two Eliashberg spectral functions side-panels, highlighting the considerably stronger electron-phonon coupling in $NbGe_2$.

In predicting the transport behavior of the group V transition metal ditetrelides using momentum-relaxing electron-phonon scattering rates, it is also useful to understand this type of scattering in the context of other scattering mechanisms present in the material. To this end, we compute the screened Coulomb electron-electron scattering lifetime ($\tau_{\text{e-e}}$), the phonon-mediated electron-electron scattering lifetime ($\tau_{\text{e-e}}^{\text{ph}}$), and the electron-phonon scattering lifetime ($\tau_{\text{e-ph}}$), different from the momentum-relaxing electron-phonon scattering lifetime in that small-angle scattering events are no longer weighted out (see Supplemental Material [20]). We plot these scattering lifetimes vs. temperature for $NbGe_2$ and $NbSi_2$ in Fig. 4(a). These scattering processes can be further classified based on whether they conserve or relax the total momentum of the electronic system. Seen in this light, the screened Coulomb and phonon-mediated electron-electron interactions are momentum-conserving, while both the electron-phonon and electron-impurity interactions are momentum-relaxing. While the timescale for direct Coulomb electron-electron scattering processes in both materials is comparable for all temperatures, the stronger electron-phonon coupling in $NbGe_2$ drastically reduces the momentum-conserving electron-electron lifetime mediated by a virtual phonon.

C. Hydrodynamic Transport

Noting that momentum-conserving scattering in $NbGe_2$ is the fastest scattering mechanism reported here for all temperatures, we investigate the potential for hydrodynamic transport in $NbGe_2$ and $NbSi_2$. Phonon-mediated anisotropic hydrodynamic flow has recently been the focus of both theoretical investigations [26–29], and direct spatially-resolved imaging in ultra-pure samples of WTe_2 for the first time [18]. To this end, it is instructive to relate the Fermi-surface averaged scattering lifetimes to a momentum-conserving (l_{mc}) and a momentum-relaxing (l_{mr}) mean-free path, using the respective Fermi velocities. Relative to the geometry's length-scale (W), these mean free paths then specify the electron flow regime we are sampling as a function of temperature [18, 30]. Figure 4(b) plots the curvature of the current density for a large range of these two non-dimensional parameters [18], illustrating that in order to observe electron hydrodynamic flow we require $l_{\text{mc}} \ll W < l_{\text{mr}}$. Superimposing the temperature-dependent mean-free paths, $l_{\text{mc}}(T)$ and $l_{\text{mr}}(T)$, for various empirical values of impurity length-scales [6], we see that in relatively clean samples (impurity mean free paths larger than 2 μm), both $NbGe_2$ and $NbSi_2$ develop curved current profiles, suggesting non-diffusive behavior for micron-scale geometries. $NbGe_2$ shows a much larger current density curvature, with a peak curvature of J_y curv. ~0.525 at ~7.5 K, while the non-diffusive behavior in $NbSi_2$ persists at higher temperatures, with a peak curvature of J_y curv. ~0.25 at ~35 K. This observation further enforces our de-

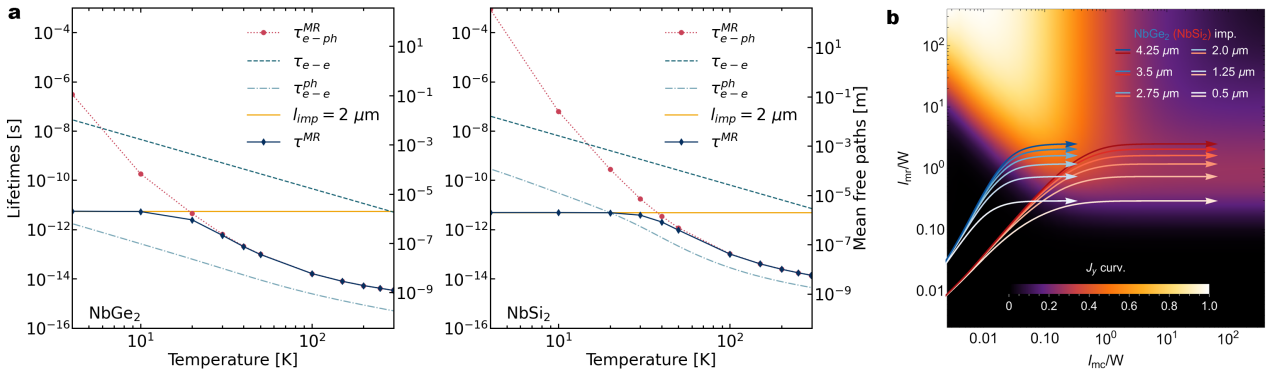

Figure 4. (a) Predicted temperature-dependent lifetimes averaged over the Fermi surface for different scattering processes in $NbGe_2$ and $NbSi_2$. The momentum-relaxing electron-phonon scattering lifetime ($\tau^{MR}_{e\text{-}ph}$) is shorter than the momentum-conserving Coulomb-mediated electron-electron scattering lifetime ($\tau_{e\text{-}e}$) until low temperatures in both materials. The phonon-mediated electron-electron scattering lifetime ($\tau^{ph}_{e\text{-}e}$) is shorter than these and is the dominant scattering process at all temperatures. At low temperatures, small-angle scattering dominates and suppresses momentum-relaxing electron-phonon scattering, as evident in comparing the electron-phonon scattering lifetime ($\tau_{e\text{-}ph}$) to $\tau^{MR}_{e\text{-}ph}$. (b) Prediction of hydrodynamic flow regimes in $NbGe_2$ (blue lines) and $NbSi_2$ (red lines) for different impurity mean-free paths. The colorscale denotes the curvature of the current profile in a channel of width W for different momentum-relaxing (l_{mr}) and momentum-conserving (l_{mc}) mean free paths. The superimposed trajectories, obtained from our *ab initio* calculations, in $NbGe_2$ (blue) and $NbSi_2$ (red), for a channel width of 1 μm, run from 298 K to 4 K.

sign principles guiding the search for material candidates to exhibit bulk hydrodynamic electron flow. Briefly, these include high-carrier density systems, for sufficient electron conduction, which couple strongly via the higher-order phonon-mediated electron-electron interaction and exhibit relatively-weak (competing) phonon-phonon scattering at the temperatures of interest. The predicted curvature value exceeds the measured and predicted result in WTe_2 making $NbGe_2$ a desirable platform for further exploration of phonon-mediated hydrodynamic transport [18].

IV. CONCLUSION

In conclusion, we have presented *ab initio* transport calculations for all six transition metal ditetrelides that crystallize in chiral hexagonal unit cells. We find excellent agreement with experiments for the subset of these materials whose electrical properties have been characterized, and at high temperatures we predict an emphasized anisotropy in the resistivity of $NbGe_2$ not observed by experiments so far. Importantly, we find that the overall comparatively high resistivities in $NbGe_2$ originate from strong electron-phonon interaction, which also leads to a higher superconducting transition temperature in this compound, as observed, for example, by Ref. [31]. Looking ahead, we observe that in moderately low temperatures above the superconducting transition, this strong electron-phonon coupling leads to pronounced momentum-conserving electron-electron scattering due to the exchange of virtual phonons, making $NbGe_2$ an ideal candidate to observe phonon-mediated hydrodynamic flow. We anticipate future work in this class of materials on the interplay and competition between hydrodynamic transport and superconductivity.

ACKNOWLEDGMENTS

We are grateful for discussions with Dr. Yaxian Wang at Harvard University and Prof. Dr. Claudia Felser at the Max Planck Institute for Chemical Physics of Solids. This work is supported by the STC Center for Integrated Quantum Materials, NSF Grant No. DMR-1231319 for development of computational methods for topological materials. G.V. and P.N. acknowledge support from the Army Research Office MURI (Ab-Initio Solid-State Quantum Materials) Grant No. W911NF-18-1-0431 that supported development of computational methods to describe microscopic, temperature-dependent dynamics in low-dimensional materials. G.V. acknowledges support from the Office of Naval Research grant on High-Tc Superconductivity at Oxide-Chalcogenide Interfaces (Grant Number N00014-18-1-2691) that supported theoretical and computational methods for phonon-mediated interactions. This work used resources of the National Energy Research Scientific Computing Center, a DOE Office of Science User Facility, as well as resources at the Research Computing Group at Harvard University. Additional calculations were performed using resources from the Department of Defense High Performance Computing Modernization Program through the Army Research Office MURI grant on Ab-Initio Solid-State Quantum Materials: Design, Production, and Characterization at the Atomic Scale (18057522). C.A.C.G. was supported by the NSF Graduate Research Fellowship Program under Grant No. DGE-1745303. P.N. is a

Moore Inventor Fellow and gratefully acknowledges support through Grant No. GBMF8048 from the Gordon and Betty Moore Foundation.

[1] G. Chang, B. J. Wieder, F. Schindler, D. S. Sanchez, I. Belopolski, S. M. Huang, B. Singh, D. Wu, T. R. Chang, T. Neupert, S. Y. Xu, H. Lin, and M. Z. Hasan, Topological quantum properties of chiral crystals, Nat. Mater. **17**, 978 (2018).

[2] J. L. Mañes, Existence of bulk chiral fermions and crystal symmetry, Phys. Rev. B **85**, 155118 (2012).

[3] S. S. Tsirkin, I. Souza, and D. Vanderbilt, Composite Weyl nodes stabilized by screw symmetry with and without time-reversal invariance, Phys. Rev. B **96**, 045102 (2017).

[4] P. Narang, C. A. Garcia, and C. Felser, The topology of electronic band structures, Nature Materials **20**, 293 (2020).

[5] D. Rees, K. Manna, B. Lu, T. Morimoto, H. Borrmann, C. Felser, J. E. Moore, D. H. Torchinsky, and J. Orenstein, Helicity-dependent photocurrents in the chiral weyl semimetal rhsi, Science advances **6**, eaba0509 (2020).

[6] U. Gottlieb, O. Laborde, O. Thomas, A. Rouault, J. P. Senateur, and R. Madar, Some transport properties of single crystals of group Va transition metal disilicides, Appl. Surf. Sci. **53**, 247 (1991).

[7] T. Hirano and M. Kaise, Electrical resistivities of single-crystalline transition-metal disilicides, J. Appl. Phys. **68**, 627 (1990).

[8] J. Lasjaunias, O. Laborde, U. Gottlieb, R. Madar, and O. Thomas, Low temperature specific heat of vsi 2, nbsi 2, and tasi 2, J. Low Temp. Phys **92**, 335 (1993).

[9] O. Laborde, J. Bossy, M. Affronte, H. Schober, and U. Gottlieb, Some properties of the phonon spectra of transition metal disilicides vsi2, nbsi2, and tasi2, Solid State Communications **126**, 415 (2003).

[10] S.-L. Wang and Y. Pan, Insight into the structures, melting points, and mechanical properties of nbsi2 from first-principles calculations, Journal of the American Ceramic Society **102**, 4822 (2019).

[11] O. Balkashin, A. Jansen, U. Gottlieb, O. Laborde, and R. Madar, Electron-phonon interaction spectra of tasi2, nbsi2 and vsi2, Solid State Communications **100**, 293 (1996).

[12] Y. Ōnuki, A. Nakamura, T. Uejo, A. Teruya, M. Hedo, T. Nakama, F. Honda, and H. Harima, Chiral-structure-driven split fermi surface properties in tasi2, nbsi2, and vsi2, Journal of the Physical Society of Japan **83**, 061018 (2014).

[13] V. N. Antonov, B. Y. Yavorsky, A. P. Shpak, V. N. Antonov, O. Jepsen, G. Guizzetti, and F. Marabelli, Electronic structure and physical properties of $nbsi_2$, Phys. Rev. B **53**, 15631 (1996).

[14] J. P. Remeika, A. S. Cooper, Z. Fisk, and D. C. Johnston, Superconductivity of single-crystal $NbGe_2$, J. Less-Common Met. **62**, 211 (1978).

[15] B. Lv, M. Li, J. Chen, Y. Yang, S. Wu, L. Qiao, F. Guan, H. Xing, Q. Tao, G.-H. Cao, and Z.-A. Xu, Type-i superconductivity in noncentrosymmetric $Nbge_2$, Phys. Rev. B **102**, 064507 (2020).

[16] E. Emmanouilidou, S. Mardanya, J. Xing, P. V. S. Reddy, A. Agarwal, T.-R. Chang, and N. Ni, Fermiology and type-i superconductivity in the chiral superconductor $Nbge_2$ with kramers-weyl fermions, Phys. Rev. B **102**, 235144 (2020).

[17] D. Zhang, T. Le, B. Lv, L. Yin, C. Chen, Z. Nie, D. Su, H. Yuan, Z.-A. Xu, and X. Lu, Full superconducting gap and type-i to type-ii superconductivity transition in single crystalline $nbge_2$, Phys. Rev. B **103**, 214508 (2021).

[18] U. Vool, A. Hamo, G. Varnavides, Y. Wang, T. X. Zhou, N. Kumar, Y. Dovzhenko, Z. Qiu, C. A. C. Garcia, A. T. Pierce, J. Gooth, P. Anikeeva, C. Felser, P. Narang, and A. Yacoby, Imaging phonon-mediated hydrodynamic flow in WTe_2 with cryogenic quantum magnetometry (2020), arXiv:2009.04477.

[19] W. Setyawan and S. Curtarolo, High-throughput electronic band structure calculations: Challenges and tools, Computational Materials Science **49**, 299 (2010).

[20] See Supplemental Material at [url] for (i) scattering lifetimes formalism; (ii) mode-resolved Fermi-surface averaged electron-phonon coupling strengths; (iii) electron hydrodynamics formalism; (iv) computational details; (v) electronic and phononic spectra, which includes Refs. [32–41].

[21] B. Bradlyn, L. Elcoro, J. Cano, M. Vergniory, Z. Wang, C. Felser, M. Aroyo, and B. A. Bernevig, Topological quantum chemistry, Nature **547**, 298 (2017).

[22] M. Vergniory, L. Elcoro, C. Felser, N. Regnault, B. A. Bernevig, and Z. Wang, A complete catalogue of high-quality topological materials, Nature **566**, 480 (2019).

[23] J. Zhang, Y.-H. Chan, C.-K. Chiu, M. G. Vergniory, L. M. Schoop, and A. P. Schnyder, Topological band crossings in hexagonal materials, Phys. Rev. Materials **2**, 074201 (2018).

[24] N. B. M. Schröter, S. Stolz, K. Manna, F. de Juan, M. G. Vergniory, J. A. Krieger, D. Pei, T. Schmitt, P. Dudin, T. K. Kim, C. Cacho, B. Bradlyn, H. Borrmann, M. Schmidt, R. Widmer, V. N. Strocov, and C. Felser, Observation and control of maximal chern numbers in a chiral topological semimetal, Science **369**, 179 (2020).

[25] P. Tang, Q. Zhou, and S.-C. Zhang, Multiple types of topological fermions in transition metal silicides, Phys. Rev. Lett. **119**, 206402 (2017).

[26] A. Levchenko and J. Schmalian, Transport properties of strongly coupled electronâĂŞphonon liquids, Annals of Physics **419**, 168218 (2020).

[27] G. Varnavides, A. S. Jermyn, P. Anikeeva, C. Felser, and P. Narang, Electron hydrodynamics in anisotropic materials, Nature Communications **11**, 4710 (2020).

[28] P. Rao and B. Bradlyn, Hall viscosity in quantum systems with discrete symmetry: Point group and lattice anisotropy, Phys. Rev. X **10**, 021005 (2020).

[29] X. Huang and A. Lucas, Electron-phonon hydrodynamics, Phys. Rev. B **103**, 155128 (2021).

[30] M. J. M. de Jong and L. W. Molenkamp, Hydrodynamic electron flow in high-mobility wires, Phys. Rev. B **51**, 13389 (1995).

[31] C. M. Knoedler and D. Douglass, Superconductivity in nbge 2 and isostructural c-40 compounds, Journal of Low Temperature Physics **37**, 189 (1979).

[32] M. J. van Setten, M. Giantomassi, E. Bousquet, M. J. Verstraete, D. R. Hamann, X. Gonze, and G. M. Rignanese, The PSEUDODOJO: Training and grading a 85 element optimized norm-conserving pseudopotential table, Comput. Phys. Commun. **226**, 39 (2018).

[33] K. F. Garrity, J. W. Bennett, K. M. Rabe, and D. Vanderbilt, Pseudopotentials for high-throughput dft calculations, Comput. Mater. Sci. **81**, 446 (2014).

[34] A. Dal Corso, Pseudopotentials periodic table: From H to Pu, Comput. Mater. Sci. **95**, 337 (2014).

[35] A. M. Rappe, K. M. Rabe, E. Kaxiras, and J. D. Joannopoulos, Optimized pseudopotentials, Phys. Rev. B **41**, 1227 (1990).

[36] N. Marzari and D. Vanderbilt, Maximally localized generalized Wannier functions for composite energy bands, Phys. Rev. B **56**, 12847 (1997).

[37] I. Souza, N. Marzari, and D. Vanderbilt, Maximally localized Wannier functions for entangled energy bands, Phys. Rev. B **65**, 035109 (2001).

[38] D. R. Hamann, Optimized norm-conserving Vanderbilt pseudopotentials, Phys. Rev. B **88**, 85117 (2013).

[39] J. P. Perdew, A. Ruzsinszky, G. I. Csonka, O. A. Vydrov, G. E. Scuseria, L. A. Constantin, X. Zhou, and K. Burke, Restoring the density-gradient expansion for exchange in solids and surfaces, Phys. Rev. Lett. **100**, 136406 (2008).

[40] N. Marzari, D. Vanderbilt, A. De Vita, and M. C. Payne, Thermal contraction and disordering of the Al(110) surface, Phys. Rev. Lett. **82**, 3296 (1999).

[41] R. Sundararaman, K. Letchworth-Weaver, K. A. Schwarz, D. Gunceler, O. Yalcin, and T. Arias, JDFTx: Software for joint density-functional theory, SoftwareX **6**, 278 (2017).